Structural Engineering and Mechanics, Vol. 28, No. 5 (2008) 525-548
DOI: http://dx.doi.org/10.12989/sem.2008.28.5.525

Quantitative nondestructive evaluation of thin plate structures using the complete frequency information from impact testing

Sang-Youl Lee

Department of Civil and Engineering, Hanyang University, 17 Haedang-Dong, Sungdong-Gu, Seoul 133-791, Korea

Guillermo Rus

Department of Structural Mechanics, University of Granada, Politécnico de Fuentenueva, 18071 Granada, Spain

Taehyo Park†

Department of Civil and Engineering, Hanyang University, 17 Haedang-Dong, Sungdong-Gu, Seoul 133-791, Korea

(Received December 13, 2006, Accepted January 23, 2008)

Abstract. This article deals the theory for solving an inverse problem of plate structures using the frequency-domain information instead of classical time-domain delays or free vibration eigenmodes or eigenvalues. A reduced set of output parameters characterizing the defect is used as a regularization technique to drastically overcome noise problems that appear in imaging techniques. A deconvolution scheme from an undamaged specimen overrides uncertainties about the input signal and other coherent noises. This approach provides the advantage that it is not necessary to visually identify the portion of the signal that contains the information about the defect. The theoretical model for Quantitative nondestructive evaluation, the relationship between the real and ideal models, the finite element method (FEM) for the forward problem, and inverse procedure for detecting the defects are developed. The theoretical formulation is experimentally verified using dynamic responses of a steel plate under impact loading at several points. The signal synthesized by FEM, the residual, and its components are analyzed for different choices of time window. The noise effects are taken into account in the inversion strategy by designing a filter for the cost functional to be minimized. The technique is focused toward a exible and rapid inspection of large areas, by recovering the position of the defect by means of a single accelerometer, overriding experimental calibration, and using a reduced number of impact events.

Keywords: inverse problem; quantitative non-destructive evaluation (QNDE); real and ideal model; finite element method (FEM); impact testing; noise effect.

† Professor, Corresponding author, E-mail: cepark@hanyang.ac.kr

1. Introduction

In the field of nondestructive evaluation (NDE), it is a common practice to characterize the internal defects using a stress wave induced by an impact or other mechanical load and interpreting the signature of the signal returned from the body. In usual NDE techniques, a great amount of information contained in the signal is neglected. This rich data may be crucial to combat the noise that hide difficult defects. This paper makes an effort to integrate all the information recorded in the measurements in a generalized processing or inversion scheme.

This work is aimed at the study of *mechanical response*, i.e., the propagation of elastic waves, which governs the well known impact testing detection techniques. The reason for the choice is that the importance of the defect as well as the remaining lifecycle are directly related to the mechanical condition, which affects most directly the propagation of waves, above other physical properties and principles that support other NDE techniques. At this point one may distinguish two ways of tackling any problem of identification (for instance impact testing, modal analysis or ultrasonics): one studying the exact problem solving direct ones in an iterative way as described in this paper, and the deduction of a simplified relationship between the excitation and the response such as transition function which substitutes the solution of a direct problem (Wooh *et al.* 1994, 1997, 2001, Eriksson *et al.* 1995, Boström *et al.* 2001, Kim *et al.* 2006).

The concept of numerical simulations in experimental NDE has previously been used successfully by a variety of investigators. Lee and Wooh (2005) identified structural damage using the combined FEM and microgenetic algorithms. Some interesting works study numerical tests for detecting defective beams or truss structures as well (Suh *et al.* 2000, Friswell *et al.* 1997, 1998, Chou and Ghaboussi 2001, Krawczuk 2002). Very simple numerical-experimental vibration analysis has been used in academic examples as well as practical civil structures (Ren *et al.* 2002, Maeck *et al.* 2001). Friswell *et al.* (1997, 1998) used simple measured eigenfrequencies comparisons from impact testing to successfully identify a defect in a clamped plate. Li *et al.* (2002) pointed out the difficulties and limitations of standard mode shape measurements for defect identification, and propose some new indexes based on the bending moment. Wendel *et al.* (1997) used training neural networks for detecting damages. On the other hand, Kimoto and Hirose (2000) pointed out the difficulties in the boundary conditions of the model, and they modeled transmitters as a distributed traction for the emitter and a weighting function on the displacements for the receiver. In this approach, a transfer function is also inserted for the transducer-specimen system, as introduced by Schmerr (1998). This transfer function is also referred to as a *linear time-shift invariant* (LTI) and is used as a Green function to average within the transducer surface. Using these techniques they obtain variations between the experimental and numerical signals of the order of 20% with respect to the maximum signal. They also introduced averaging of computations to enhance the results. Zhao *et al.* (1995) used the velocity instead of the displacement to model the receiver. Some efforts were made by Rus *et al.* (2004) to study which boundary conditions correctly simulate the effect of the transducer on the specimen model. The basis for this hypothesis and the linearity of the system are reviewed in the present paper.

The existing methods for damage localization mainly focus on finding differences between the undamaged and the damaged structure from mode shapes, deformed shapes, etc. Backtracking techniques like finding the load vector that gives an unchanged response are successfully examined by Bernal (2002). Some experimental results are shown by Marty *et al.* (2000) regarding lamb waves in plates to search defects modeled by thickness variations.

On the other hand, the identifiability is an issue that has been addressed thoroughly in statistics and mathematics, and has been used widely in chemistry and physics. However, in the field of nondestructive testing, only observational comments have been made about the issue. Liu *et al.* (1996) discussed as identifiability the relationship between the number of measurements and the number of degrees of freedom only to establish a necessity condition. In addition, the theoretical issue of the modelization of the receivers has never been explicitly studied in much detail. In particular, the mechanical interactions between the receiver and the specimen may need to be studied in detail. Therefore, some work is carried out here on the analytical formulation associated with mechanical coupling receiver and specimen based on the concepts described by Rus *et al.* (2004). Then, the forward and inverse procedures is presented to identify damage in steel plates by combining the FEM and a parametrization-minimization scheme, and using impact loading data.

In this paper, a theoretical model is developed for damage detection in plate structures. Some experimental results which support this theory are described subsequently. The experimental work is implemented by processing the experimental signal and then synthesizing the signal using an FEM procedure. Using the developed formulation, the residual and cost functional is minimized for the parameters that characterize the defect and act as unknowns of the inverse problem. The identification is carried out to efficiently, taking into account the effects of noise and other uncertainties such as the exact mechanical properties of the plate material.

2. The system model

First and foremost, we define in Fig. 1 a generic impact testing system and its components for nondestructive evaluation (NDE) of a structure, in which the time functions $s_m^{(I)}(t), s_{mn}^{(R)}(t)$, and $s_{mn}^{(O)}(t)$ respectively denote the signals generated by the impact, those transmitted to the receiver, and those recorded by an oscilloscope. The parenthesized superscripts (I), (R), and (O) denote impactor, receiver, and output, respectively. In this system, we consider generating signals by multiple impacts at various points and receiving the signals from multiple locations using an array of transducers. For a testing with m impact events recorded by n transducers, we obtain a total number of $m \times n$ signals.

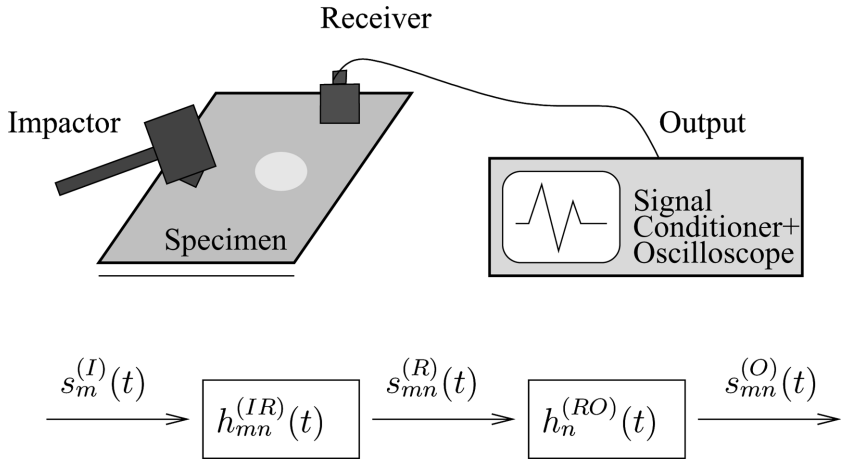

Fig. 1 Scheme of a typical impact testing system

2.1 Assumptions

We make the basic assumptions as follows:

1. In our model, the signals generated by the impactor are described by prescribing the pressure boundary conditions $q_i(x, t)$. The validity of this assumption was studied by Rus *et al.* (2004) by comparing the results between the two extreme cases of Neumann and Dirichlet boundary conditions.
2. We assume that the pressure induced by impact, $q_i(x, t)$, is distributed uniformly over the area of contact (i.e., does not depend on x). Thus, the impact pressure can be prescribed by multiplying the constant pressure q_i and its phase $\varsigma(t)$ or time delay
$$q_i(x,t) = q_i\varsigma(t) \tag{1}$$
3. We assume that the signal output from the receiver is the time average of displacements (or accelerations) of the points on Γ_n, the area of contact between the specimen and the receiving transducer, i.e.
$$u_i(t) = \int_{\Gamma_n} u_i(\Gamma, t)d\Gamma \tag{2}$$
4. Shear stresses cannot be sustained on the specimen-impactor or the specimen-receiver boundaries. In other words, we only consider the normal components
$$\begin{aligned} s_m^{(I)}(t) &= n_i q_i(x,t) && \text{(Impactor)} \\ s_{mn}^{(R)}(t) &= n_i u_i(t) = n_i \int_{\Gamma_n} u_i(\Gamma, t)d\Gamma && \text{(Receiver)} \end{aligned} \tag{3}$$
where n_i is the surface normal (assumed constant on a small area of the plate) and Γ_n is the contact area between the receiver and the specimen.
5. We assume that the system is linear time invariant (LTI). In other words, for the system described in Fig. 1, the relationships between the signals can be expressed as the convolutions in the time domain as follows
$$\begin{aligned} s_{mn}^{(O)}(t) &= h_n^{(RO)}(t) * s_{mn}^{(R)}(t) \\ s_{mn}^{(R)}(t) &= h_{mn}^{(IR)}(t) * s_m^{(I)}(t) \end{aligned} \tag{4}$$
where $h_{mn}^{(IR)}(t)$ is the response function of the specimen under test and $h_n^{(RO)}(t)$ is the electromechanical response of the receiver and acquisition system. The convolution product (*) is defined in the standard way as
$$A(t) * B(t) = \int_{-\infty}^{\infty} A(\tau)B(\tau - t)d\tau \tag{5}$$
It is possible to assume the linearity of the response function of the specimen since the excitation magnitude is small compared to the elastic constitutive range of the damaged material, since the impact testing loads are negligible in comparison witho the damaging loads. The electromechanical coupling between the transducer and specimen is assumed to be LTI as shown in the next section.

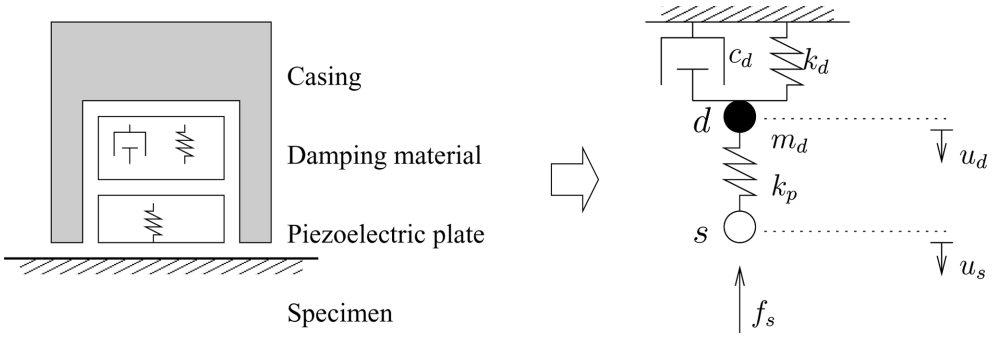

Fig. 2 Diagram of the physical transducer model

2.2 The electromechanical responses

In many practical applications, a dynamic system response can be measured using a commercial transducer such as piezoelectric accelerometers or displacement sensors which convert mechanical motions into electrical signals. The behavior of a transducer may be modeled by a complex electromechanical system by considering all the design details of the system. However, a number of assumptions allow us to simplify the model by establishing linear relationships.

We consider a transducer consisting of the linear components shown in Fig. 2, i.e., a transducer constructed with a piezoelectric plate, damping material and the casing. Such a transducer can be approximately characterized by the following properties: the constant k_p is the stiffness of the piezoelectric plate, k_d the stiffness of the equivalent spring of the damper, c_d the damping coefficient of the damper, m_d the lumped mass attributed to the damper, and f_s is the force acting on the surfaces between the specimen and the transducer. The variables u_s and u_d denote the displacements of the specimen and the damper, respectively. Notice that these are the displacements of the two surfaces of the piezoelectric plate in the transducer. The pair $\{u_s, f_s\}$ defines the mixed boundary condition at the specimen-transducer contact area.

The equilibrium equation for this model can be written as

$$m_d\ddot{u}_d(t) + c_d\dot{u}_d(t) + k_d u_d(t) + k_p u_d(t) = k_p u_s(t) \tag{6}$$

It is noted that the displacement can be decomposed into the harmonics using the Fourier decomposition

$$u(t) = \int_{\omega} U(\omega)e^{j\omega t}d\omega \tag{7}$$

where ω is the angular frequency, $U(\omega)$ the Fourier transform of $u(t)$, and j is the unit imaginary number. This model allows to rewrite the equilibrium equations in the form

$$U_d(\omega) = A_1(\omega)U_s(\omega) \tag{8}$$

where

$$A_1(\omega) = \frac{k_p}{-m_d\omega^2 + jc_d\omega + k_d + k_p} \tag{9}$$

and $A_i(\omega)$, the inverse transforms of $\alpha_i(t)$, are the complex constants in the remaining of the paper. The deformation of the piezoelectric plate can be expressed by the difference between the displacements of its surfaces as

$$U_d - U_s = A_2 U_s \tag{10}$$

where

$$A_2(\omega) = \frac{m_d\omega^2 - jc_d\omega - k_d}{-m_d\omega^2 + jc_d\omega + k_d + k_p} \tag{11}$$

Without losing the generality, the output signal $s_{mn}^{(O)}(t)$ produced by the piezo-material can be assumed to be linearly proportional to the deformation as follows (since, given a fixed frequency, the displacement, velocity and acceleration are just proportional to each other by a constant complex factor)

$$s_{mn}^{(O)}(t) = \alpha_3(u_d - u_s) \tag{12}$$

From Eq. (10), this can be simply written as

$$s_{mn}^{(O)}(t) = \alpha_4 u_s, \quad \alpha_4 = \mathcal{F}^{-1}\{A_2 A_3\} \tag{13}$$

This means that the relationship between the displacements can be numerically modeled without considering transducer models for the recorded output signals always follow linear relationships. For this condition, it is always possible to group the signals into a single transfer function of Fourier type using a proper amplitude rescaling and phase shifts. Consequently, it is not necessary to predict the transfer function theoretically, but it can be estimated experimentally at the stage of calibration.

3. Forward procedure

3.1 Measurement data

In order to eliminate the uncertainties in the impact excitation forces or other coherent noises, a convolution-based procedure is designed by comparing the responses of a structure in its undamaged and damaged states. Recall that Eq. (4) represents the linear relationships between the output signal $s_{mn}^{(O)}(t)$ recorded by the n-th receiver and the corresponding impact signal $s_m^{(I)}(t)$ generated by the m-th impact event. Looking at Fig. 3, these equations can be rewritten as

$$s_{mn}^{(O)}(t) = h_n^{(RO)}(t) * h_{mn}^{(IR)}(t) * s_m^{(I)}(t) = g_{mn}(t) * h_{mn}^{(IR)}(t) \tag{14}$$

where

$$g_{mn}(t) = s_m^{(I)}(t) * h_n^{(RO)}(t) \tag{15}$$

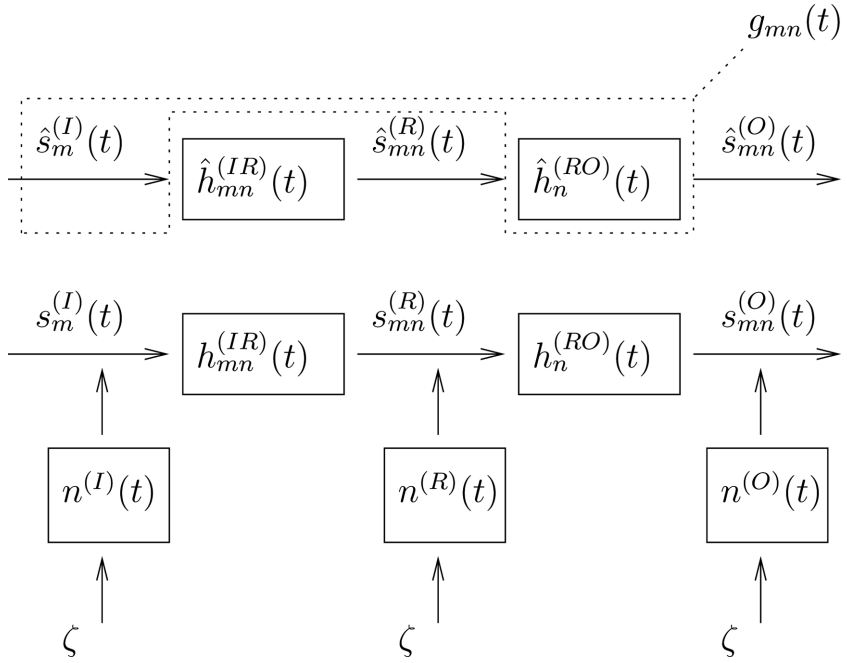

Fig. 3 Chart of real and theoretical model of the NDE system

This allows us to describe the response of the complete testing system by a single equation. Taking the inverse of Eq. (15), we obtain the response of the specimen as

$$h_{mn}^{(IR)}(t) = g_{mn}^{-1}(t) * s_{mn}^{(O)}(t) \tag{16}$$

which is a property independent of the input signal or intrinsic coherent noises coming from the system. The transfer function $g_{mn}(t)$ can now be used as the input excitation function in our numerical model to obtain the output signal $s_{mn}^{(O)}(t)$ by convolving it with the specimen response $h_{mn}^{(IR)}(t)$. Recall that this is true as long as the model is linear, i.e., it admits the principle of superposition.

3.2 Real and theoretical models

It becomes necessary to study the difference between the real and theoretical models in order to assert later some hypothesis of the model. For the signals shown in Fig. 3, the real model is described by Eq. (14), whereas the theoretical model can be represented by the relationship

$$\hat{s}_{mn}^{(O)}(t) = \hat{h}_n^{(RO)}(t) * \hat{h}_{mn}^{(IR)}(t) * \hat{s}_m^{(I)}(t) \tag{17}$$

where the hats are used to denote the theoretical values.

In our study, we assume that the real function $f(t)$ is linearly proportional to the sum of the theoretical function $\hat{f}(t)$ and the bandpass-filtered noise

$$f(t) = z(\hat{f}(t) + n(t) * \zeta(t)) \tag{18}$$

where $n(t)$ is the noise function, and z is the "scaling parameter" or "gain". The output or input signals depend on the variation of applied pressure which can be compensated by an arbitrary choice of the constant z. We assume that the bandpass-filter $\zeta(t)$ has Gaussian probability distribution with zero average and unity variance. In other words, this represents a random white noise of unit magnitude. Note that this function allows us to neglect the phase and sign information in our formulation. Thus, the aforementioned signals and transfer functions can be written in the form

$$\begin{aligned} s_{mn}^{(O)}(t) &= z^{(O)}(\hat{s}_{mn}^{(O)}(t) + n^{(O)}(t) * \zeta(t)) \\ h_{n}^{(RO)}(t) &= z^{(RO)}(\hat{h}_{n}^{(RO)}(t) + n^{(RO)}(t) * \zeta(t)) \\ h_{mn}^{(IR)}(t) &= z^{(IR)}(\hat{h}_{mn}^{(IR)}(t) + n^{(IR)}(t) * \zeta(t)) \\ s_{m}^{(I)}(t) &= z^{(I)}(\hat{s}_{m}^{(I)}(t) + n^{(I)}(t) * \zeta(t)) \end{aligned} \tag{19}$$

Substituting Eq. (19) into Eq. (14) and after neglecting the higher order terms of the noise, we obtain

$$\begin{aligned} z^{(O)}\hat{s}_{mn}^{(O)}(t) + z^{(O)}n^{(O)}\zeta = {} & z^{(RO)}\hat{h}_{n}^{(RO)}z^{(IR)}\hat{h}_{mn}^{(IR)}z^{(I)}\hat{s}_{m}^{(I)} + z^{(RO)}n^{(RO)}z^{(IR)}\hat{h}_{mn}^{(IR)}z^{(I)}\hat{s}_{m}^{(I)}\zeta \\ & + z^{(RO)}\hat{h}_{n}^{(RO)}z^{(IR)}n^{(IR)}z^{(I)}\hat{s}_{m}^{(I)}\zeta + z^{(RO)}\hat{h}_{n}^{(RO)}z^{(IR)}\hat{h}_{mn}^{(IR)}z^{(I)}n^{(I)}\zeta \end{aligned} \tag{20}$$

The equality condition in this equation should be independently carried out for the group of terms with and without noise. Equating the terms without noise and using Eq. (17), we obtain

$$z^{(IR)} = \frac{z^{(O)}}{z^{(RO)}z^{(I)}} \tag{21}$$

This unifies the pressure-dependent scaling factor. Equating the terms with the first order noise, we obtain the following relationship

$$\frac{n^{(IR)}}{\hat{h}_{mn}^{(IR)}} = \frac{n^{(O)}}{\hat{h}^{(O)}} + \frac{n^{(RO)}}{\hat{h}_{n}^{(RO)}} + \frac{n^{(I)}}{\hat{s}_{m}^{(I)}} \tag{22}$$

3.3 Finite element method

The forward problem is formulated using the finite element analysis. In a finite element formulation, the stiffness matrix of a structural system is expressed in terms of its material properties, geometry, and boundary conditions. In numerical approach for detecting damage, there are two different methods to define the extent of damage. The first is the reduction of material properties (Young's modulus or Poisson's ratio) of a specific element. For example, 20% damage at an element implies that there will be 20% reduction of Young's modulus or Poission's ratio (Gudmudson 1982, Christides and Barr 1984). The other method is to define the *stiffness reduction factor* quantifying the severity of the damage. For example, when a damage occurs in a structure, the stiffness matrix in its damaged state can be represented as the sum of the element stiffness

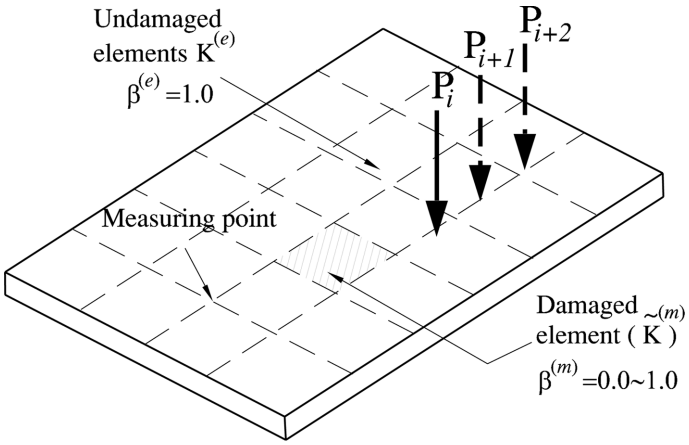

Fig. 4 Finite element model of plates subject to impact load with one damaged element. The locations of loads and measurements are assumed arbitrary in the figure

matrices multiplied by a reduction factor representing the damage (Mares and Surace 1996, Au *et al.* 2003). Although it is not the limitation of the approach in general, we have a restricted study scope in this paper, in that the damage is defined as the stiffness reduction factor at local areas as shown in Fig. 4. In particular, the structure is discretized into a set of finite elements categorized into undamaged and damaged states of different degradation levels. For such a model, the global stiffness matrix of the m-th damaged element can be expressed as

$$\tilde{\mathbf{D}}^{(m)} = \beta^{(m)}\mathbf{D}^{(m)} \tag{23}$$

where $\beta^{(m)}$ is the *stiffness reduction factor* and $\mathbf{D}^{(m)}$ is the stiffness in its original (undamaged) state. Note that the tilde symbol is used to denote the variables in their damaged state. The stiffness matrix of the damaged element in the local coordinates can now be written as the volume integral of the form

$$\tilde{\mathbf{K}}^{(m)} = \beta^{(m)} \int_V \mathbf{B}^{(e)T} \tilde{\mathbf{D}}^{(m)} \mathbf{B}^{(e)} d\Omega \tag{24}$$

where $\mathbf{B}^{(e)}$ is the strain-displacement matrix of the element e, and the superscript T denotes the transpose operator. Note that $\mathbf{B}^{(e)}$ is a property that is independent of damage, thus it is applicable to all the elements e, whether damaged or undamaged.

The governing equation of motion of the system is written in the form

$$\mathbf{K}\ddot{\mathbf{u}} + \mathbf{K}\mathbf{u} = \mathbf{P}_i, \qquad i = 1, \ldots, n \tag{25}$$

where $\mathbf{u}$ and $\ddot{\mathbf{u}}$ are the displacement and acceleration vectors, $\mathbf{M}$ and $\mathbf{K}$ are the mass and stiffness matrices and $\mathbf{P}_i$ is the time history of the n iterative applied impact load, respectively. To advance the solution of this equation in time, we use Newmark's direct integration method (Bathe 1996, Xiang *et al.* 2007), in which the time dimension is represented by a set of discrete points with equal time increment of Δt. The following naming convention is adopted: the value of a function $\xi(t)$ at time $t = n\Delta t$ is denoted by the index n as

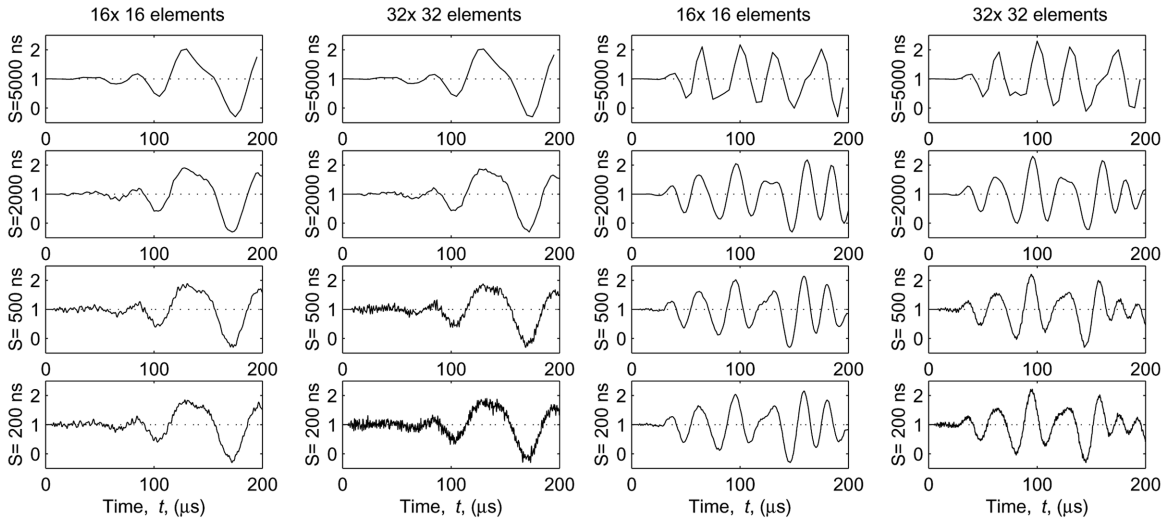

Fig. 5 Simulated signal at a single accelerometer/impact point by FEM procedure for a variety of choices of the time step and element size in the FEM procedure. Central frequency of the input pulse: 15 kHz on the left hand side and 30 kHz on the right hand side

$$\xi(t) = \xi(n\Delta t) = \xi[n], \qquad n = 0, \ldots, N \tag{26}$$

where $N + 1$ is the total number of temporal discretization points for the entire duration of time T_d.

Three parameters have to be combined in order to find the best compromise with the computational cost and attain the needed precision and convergence in the results. These magnitudes are the sampling rate or time step S, which are tested from 200 ns to 5000 ns, the number of elements in the discretization of the problem, which vary from 16×16 to 32×32 and the frequency contents of the pulse applied as mechanical input (with Gaussian distribution and a central frequency from 15 kHz to 30 kHz), which set an upper limit to the time resolution of any output computation after the convolution. To analyze the computations shown in Fig. 5 it is necessary to find the conditions for which the computations reach the convergence, in the sense that the signal becomes independent of the sampling rate and mesh refinement. In the case of 15 kHz, the following set of figures are below 5% difference, which allows to assume achieved convergence (apart from oscillatory problems that will be later eliminated after the convolution): S = 200 ns (16×16), S = 200 ns (32×32), S = 500 ns (32×32), and S = 500 ns (32×32), respectively. In the case of 30 kHz, the following set of figures are assumed to converge: S = 500 ns (32×32) and S = 200 ns (32×32). Since we should guarantee a precision within 5% for central input frequency of 30 kHz, we choose a time step of 500 ns and a mesh of 32×32 elements.

4. Inverse procedure

4.1 Parameterization

In an inverse problem, we seek information such as the size and orientation of defects based on

the known forward problem. The actual parameterization procedure can be complicated due to the entangled relationships in many hypothetical arguments. Many inverse problems are ill-posed: solutions may not exist, they could be unstable and non-converging, or there may exist multiple solutions. This is true especially when we are dealing with a large number of parameters. Inverse problems could be solved by narrowing the scope down to a manageable scale and properly parameterizing the problem using a set of parameters (p_g) with a reduced number of variables (g). Choosing the proper parameters is a critical step that determines the robustness, convergence, sensitivity and the dependence on the measurement errors. In this work we adopt a simple two parameter-system: the horizontal (p_1) and vertical (p_2) coordinates of the center of the defect.

4.2 Residual

We introduce the *residual vector* **R** in order to quantify the misfit or discrepancy between the ideal measurements and theoretical predictions. While the prediction is based on a set p_g consisting of g parameters, the ideal measurement data are represented by the corresponding set p_g^r where the superscript r denotes the real defects. In general, residuals are defined by comparing the two (real and ideal) output signals $s^{(O)}(t)$. But, in our definition, we use the system response $h^{(IR)}(t)$ or its frequency domain representation $H^{(IR)}(\omega)$ in the definition of the residual. Recall that the theoretical response function is expressed in the frequency domain as

$$\hat{H}_{mn}^{(IR)}(p_g^r, Z) = \frac{1}{Z} H_{mn}^{(IR)} + N_{mn}^{(IR)} \Lambda \tag{27}$$

where $\Lambda = \Lambda(\omega)$ is the frequency response of the band-pass filter $\zeta(t)$ that affects the random noise process $N_{mn}^{(IR)}$ and Z is that of the amplitude compensation variable $z = z^{(IR)}(t)$.

The predicted data, which will be denoted by $\tilde{H}_{mn}^{(IR)}(p_g)$, are resulted from the computation using a set of trial values for the parameters p_g. The discrepancy $D_{mn}(p_g, Z)$ is defined as the difference between the trial and measured values, that is

$$D_{mn}(p_g, Z) = \tilde{H}_{mn}^{(IR)}(p_g) - \frac{1}{Z} H_{mn}^{(IR)} \tag{28}$$

Then the prediction can be expressed as

$$\tilde{H}_{mn}^{(IR)}(p_g) = \frac{1}{Z} H_{mn}^{(IR)} + D_{mn}(p_g, Z) = \hat{H}_{mn}^{(IR)}(p_g^r, Z) + D_{mn}(p_g, Z) + N_{mn}^{(IR)} \Lambda \tag{29}$$

In this equation, the difference between the ideal ($\hat{H}^{(IR)}$) and computed ($\tilde{H}^{(IR)}$) models, due to numerical and model errors, is taken into account as part of the noise ($N^{(IR)}$) by substituting Eq. (27) intp Eq. (28). Note that the sign of the noise is neglected since N is a symmetric stochastic process of zero mean. Now we define the residual vector **R** in terms of the discrepancy as

$$\mathbf{R}(p_g, Z) = R_{mn}(p_g, Z) = W[D_{mn}(p_g, Z)] = W\left[\tilde{H}_{mn}^{(IR)}(p_g) - \frac{1}{Z} H_{mn}^{(IR)}\right] \tag{30}$$

where $W = W(\omega)$ is a user selectable filter. The filter can be defined for giving more weight on certain important frequencies while reducing or eliminating the others. An optimimum design of this filter falls beyond the scope of the present experimental work, and has been previously

developed in more detailed by the authors (Rus *et al.* 2006), with the goal of maximizing the Probability of Detection (POD).

4.3 Undamaged specimen for compensation

A measurement $\mathring{S}_{mn}^{(O)}$ and a numerical prediction $\mathring{\tilde{H}}_{mn}^{(IR)}$ are made for a undamaged specimen in order to calibrate G for some coherent noise, amplitudes, transfer functions of the NDE system and the input signal (the undamaged specimen is referenced by $\circ$). The latter is defined in Eq. (31) as the average of G_{mn} (see Eq. (16)) for every impactor and receiver (N^m and N^n respectively) computed from the undamaged specimen. The motivation of the average is to reduce the coherent noise coming from the excitation signal by a factor $\sqrt{N^m N^n}$ in assuming Gaussian distribution of the noise.

$$G = \frac{1}{N^m N^n} \sum_{m,n} (\mathring{\tilde{H}}_{mn}^{(IR)})^{-1} \mathring{S}_{mn}^{(O)} \tag{31}$$

Recalling Eq. (29) for the undamaged specimen (where D_{mn} vanishes by definition), it is possible to include the amplitude factor Z inside G. Provided that Z is the same for the undamaged and defective tests, the factor is effectively eliminated for the whole formulation

$$\mathring{\tilde{H}}_{mn}^{(IR)} = \frac{1}{Z} \mathring{H}_{mn}^{(IR)} = \frac{1}{Z} (G')^{-1} \mathring{S}_{mn}, \qquad G = ZG' \tag{32}$$

It has been explained that the measured quantity that defines the discrepancy and the residual $\mathbf{R}$ is the transfer function $H_{mn}^{(IR)}$ instead of the directly measurable signal $S_{mn}^{(O)}$ (which would define the analogous residual $\mathbf{R}'$). Both residuals are nevertheless related by a multiplicative factor $G/\mathring{S}_{mn}^{(O)}$, where $G = G(\omega)$ is the frequency domain form of $g(t)$

$$R'_{mn} = W\left[\left(\frac{S_{mn}^{(O)} - \mathring{S}_{mn}^{(O)}}{\mathring{S}_{mn}^{(O)}} \right) - \left(\frac{\tilde{H}_{mn}^{(IR)}(p_g) \dfrac{G}{G_{mn}} - \mathring{\tilde{H}}_{mn}^{(IR)}}{\mathring{\tilde{H}}_{mn}^{(IR)}} \right) \right] = \frac{G}{\mathring{S}_{mn}^{(O)}} R_{mn} \tag{33}$$

4.4 Cost functional

We finally define a cost functional J in terms of the former residual R in a quadratic sense, which is also a least squares sense. This definition is meaningful from the statistical point of view, as well as from a space theory, since is minimizes distances in an Euclidean sense. The cost functional is hence defined as in Eq. (34) for the case of the discrete frequency domain.

$$J = \frac{1}{2} \mathbf{R}^T \overline{\mathbf{R}} = \frac{1}{2} \|\mathbf{R}\|^2, \quad J(p_g, z) = \frac{1}{2} \sum_{j=-\infty}^{+\infty} R_{mn}(p_g, z, \omega_j) \overline{R}_{mn}(p_g, z, \omega_j) \tag{34}$$

where T stands for the transpose in vectorial notation and $\overline{R}$ means the conjugate of the complex magnitude R. In the appendix, the proof of equivalence between time and frequency domain definitions of the cost functional J is made, which for the case of a synthetic array of impactors m or receivers n which can be weigthed by v_{mn}, and applied to the previously defined residual $\mathbf{R}$ yields

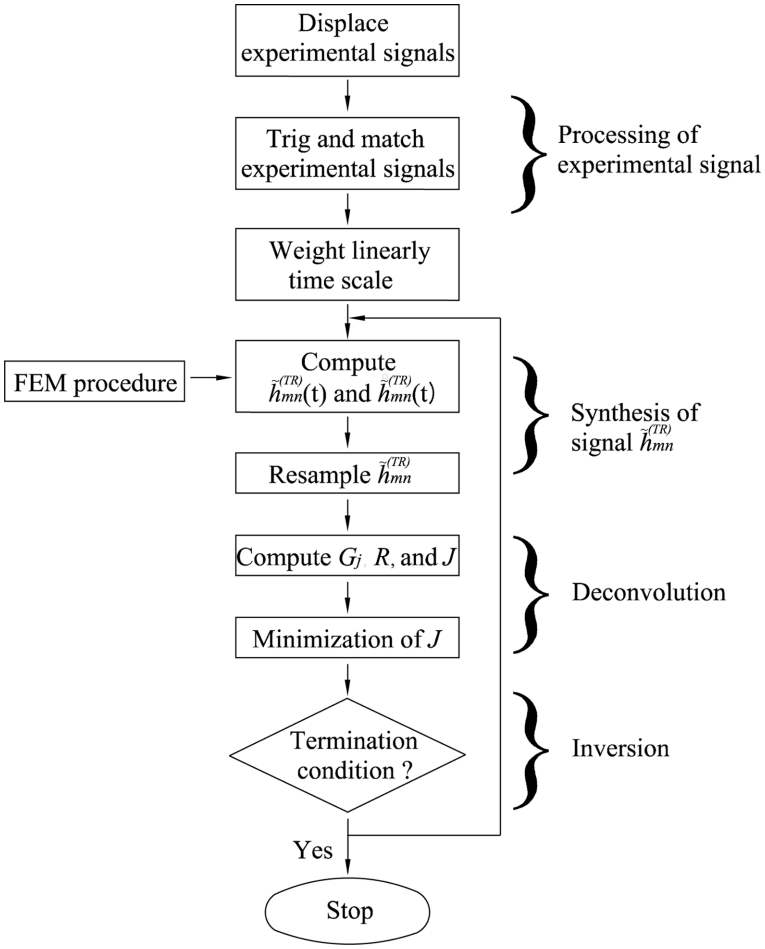

Fig. 6 Flow chart of the damage identification procedure

$$
\begin{aligned}
J &= \frac{1}{2T}\sum_{m,n} v_{mn}^2 J_{mn} \\
&= \frac{1}{2N}\sum_{m,n}\int_0^T [w(t) * v_{mn}(\tilde{h}_{mn}^{(IR)}(t) - h_{mn}^{(IR)}(t))]^2 dt \\
&= \frac{1}{2N^2}\sum_{m,n,j} |v_{mn} W(\omega_j)|^2 \left|\tilde{H}_{mn}^{(IR)}(\omega_j) - H_{mn}^{(IR)}(\omega_j)\right|^2
\end{aligned} \tag{35}
$$

The theory described above is implemented for the evaluation of a defect in a specimen using the recorded output signal in the order described in the ow chart on Fig. 6. The process of the experimental defect identification can be divided into four steps: *preprocessing of the experimental signal*, *synthesis* of the signal $\tilde{h}^{(IR)}$, *deconvolution*, and *inversion*. At the first step, the recorded experimental signals are displaced to zero mean over the first 25 μs. This is done to avoid inconsistences during Fourier decompositions. Then, they are triggered from the undamaged

specimen at a level of 1% of the RMS of the signal to define a coherent time origin. Next, the experimental signals of the undamaged and defective specimen are matched by adjusting the time shifting, the amplitude and the translation. Here, the time window is only considered between 0 and 100 μs. We will deal with the details of those in paragraph 5.2. Finally the timescale is weighted linearly by a declining ramp along the time window. A period of 1000 μs of zero-signal is padded after the time window. This is done in order to condition the time to frequency domain conversions.

In the *synthesis* of the signal $\tilde{h}^{(IR)}$, we first compute $\tilde{h}^{(IR)}_{mn}(t)$ and $\overset{\circ}{\tilde{h}}{}^{(IR)}_{mn}(t)$ by the explicit FEM procedure. The sampling rate is 500 ns, the time period is 100 μs and the mesh is defined by 32×32 elements as discussed in section 3.3. The load is defined as an unit magnitude full load during the first time sample (duration 500 ns), and the output is convolved with a function with Gaussian distribution of frequency components of average and bandwidth 50 kHz to filter and precondition the signal. Then, we resample the computed signal $\tilde{h}^{(IR)}_{mn}(t)$ by a factor $\alpha = p/q$. A polyphase implementation has been used with a sampling up between $p = \times 190$ and $\times 210$ (200 by default), and a sampling down of $q = \times 200$, with an oversampling of $N = \times 10$, and including an anti-aliasing (lowpass) FIR filter, a compensation for signal delay after the filter and a Kaiser window with $\beta = 5$ from following equation

$$w_n = I_0(\beta\sqrt{1 - n^2/m^2})/I_0(\beta) \tag{36}$$

where I_0 is a zero order modified Bessel function.

For the experimental signal, we weight linearly the timescale, trig the signal from the undamaged specimen at 10% of the RMS of the signal, and match signals from the defective specimen by time shifting to minimize the RMS difference between undamaged and defective signals over the first 50 μs. In the *deconvolution*, we implement four substeps: (1) to compute G_j as defined in Eq. (33) according to the standard definition of the convolution product in Eq. (5); (2) to define a weight $W_j = G_j * W_j'$, where W_j' has a constant default value, (3) to compute the residual $\mathbf{R}$ (4) to compute the cost functional J. In the *inversion*, an iterative minimization algorithm of the cost functional J performs the steps *Synthesis* to *Deconvolution* at each iteration, in which p_g is varied according to the chosen maximization algorithm. In this case, since the purpose is not to test the maximization algorithm, but to use a slow and safe method, a full search maximization algorithm is used, which evaluates at a grid of points spaced by the finite element spatial size.

5. Experimental results

5.1 Experimental model

The specimen consists of a 177×177 mm steel plate of 3 mm thickness clamped on one side. The defect is a 100% thickness square perforation of size 22.1×22.1 mm placed at the coordinates depicted in Fig. 7. It should be pointed out that this type of defect of thickness reduction is the most simple one, and it does not limit the generality of the theoretical formulation in this paper. The experimental data generation and retrieval is implemented as follows. The wave is excited by a specifically manufactured hammer with a hardened steel sphere that provokes an impact on the surface of the specimen with a fixed speed every time. The impact speed is generated by gravity in

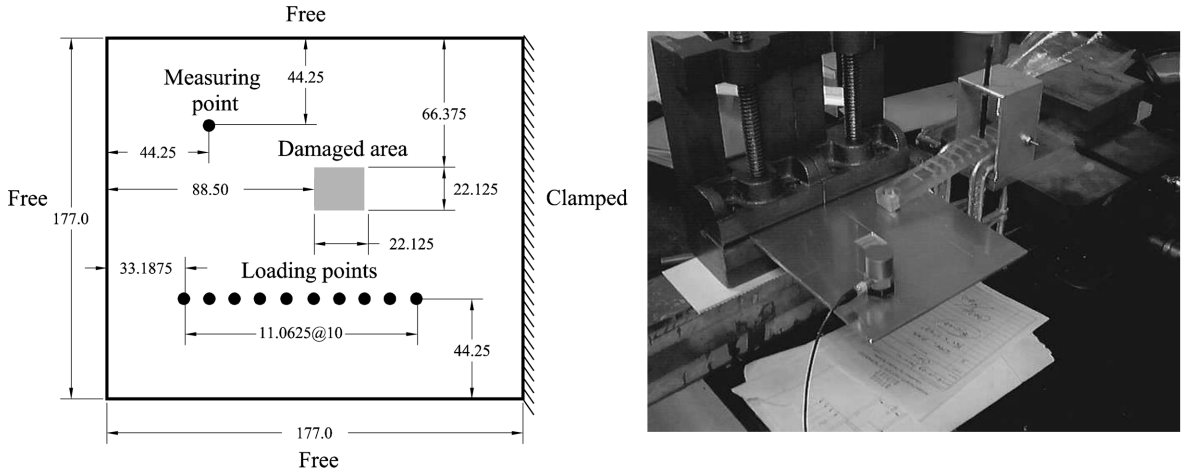

(a) Dimension of plate with defect (unit:*mm*) (b) Experimental setup

Fig. 7 Scheme of the specimen with defect, and impact testing experimental setup

Table 1 Characterization of the experimental setup apparatus

Accelerometer		**Oscilloscope**	
Model	PCB 353B33	Model	Agilent 54624A
Voltage sensitivity	103.1 mV/g	Amplitude division	5 V/div
Frequency range (±3 dB)	0.35-12000 Hz	Time division	100 μs/div
Measure range	50 g	Time trigger delay	−400 μs
Transverse sensitivity	0.1%	Trigger level	160 mV
Resonant frequency	26 kHz	Averaging	1×
Output impedance	≤100Ω		
Weight	27 g	**Signal conditioner**	
Sealing	Titanium	Model	PCB 482A20
Sensitivity (Hz)	Dev. (%)	Gain	×1
10	0.4		
15	0.2	**Impact hammer**	
30	−0.4	Material	Stainless steel
50	−0.3	Heigth	4 mm
100	0.0	Geometry	Spherical r = 1/4”
300	0.2		
500	0.2		
1000	0.2		
3000	2.5		
4000	3.5		

a free fall from a controlled height. The impact point is moved ten times to generate ten measurements (m = 1 – 10) with identical impact schemes, at the ten points depicted in Fig. 7. The data retrieval is made with just one accelerometer (n = 1), placed as depicted in Fig. 7, in order to alter as little as possible the mass distribution of the specimen and its mechanical behavior. The

signal from the accelerometer is preconditioned and recorded in a digital oscilloscope. The hardware is characterized in Table 1.

5.2 Matching experimental signals

Since the recordings from the undamaged and damaged states come from different specimens and tests, and since no triggering system has been coupled to the actuator, there is an unknown time shifting between them, an abscissas shifting, as well as an amplitude scale variation originated both at the emitter and the receiver. To reduce these unknowns as far as possible, a procedure to adjust them has been designed by trial-error, and is detailed later. It consists of two phases, and only the matched signals are treated in the remaining of the paper. First of all, the first positive extremum is sought in both signals (damaged and undamaged states) that exceeds 20% of the peak to peak amplitude, and the delay is determined between the extrema. Then the last negative extremum is sought before the latter point, and a new delay is determined. The defect signal $s_n^{(O)}(t)$ is shifted by the average of the last two time delays. Secondly, the values of the signals are evaluated at the extrema, and the defect signal is rescaled and displaced to match both extrema. Next, starting from the previous preconditioned signals, a penalty functional P is defined as the time-integral of the squared difference between signals. The functional is weighted by a declining linear ramp in order to give more importance to $t = 0$. The physical reason for doing it is that the deviation of the signal due to the defect appears after a certain time lag and therefore increases gradually, so we should induce matching with more weight before that deviation. Three parameters are defined to modify the defect signal, a time shifting p_1, an amplitude rescale p_2 and an abscissas displacement p_3. An optimization is performed by a BFGS (Dennis and Robert 1983, 1996) algorithm to find the value

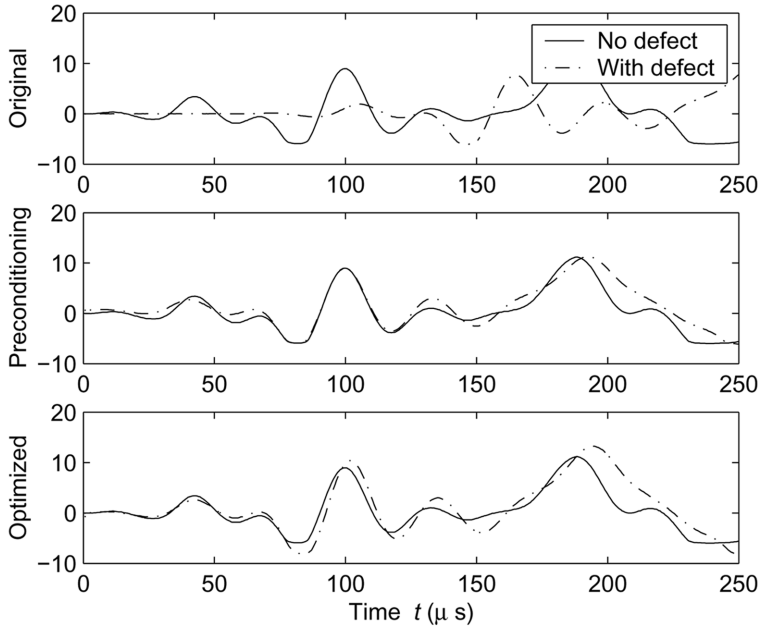

Fig. 8 Example of the stages in the procedure for matching a recorded single signal (case of measurement number $m = 10$)

of the latter parameters that minimize P

$$\min_{(p_1,p_2,p_3)} P(p_1,p_2,p_3) = \int_0^{100\mu s} W(t)(\mathring{s}_n^{(O)}(t) - s_n^{(O)}(t;p_1,p_2,p_3))^2 dt \tag{37}$$

An example of the performance of the stages of this procedure is shown in Fig. 8 for one of the measurement signals.

5.3 Synthetic signal and inversion

Fig. 9 shows the synthetic signal as well as the residual and its components for different choices of time window, tested between 0 – 50 μs and 0 – 500 μs. The case of 0 – 100 μs is chosen as the similarities between synthetic and real signal seem to be best. This decision is based on the features shown in the residual $\mathring{S} * (H * g/g_m - \mathring{H})/\mathring{H}$ (center), which is smallest and smoothest, and the corresponding transfer function, which is most coherent (the transfer function shows the least

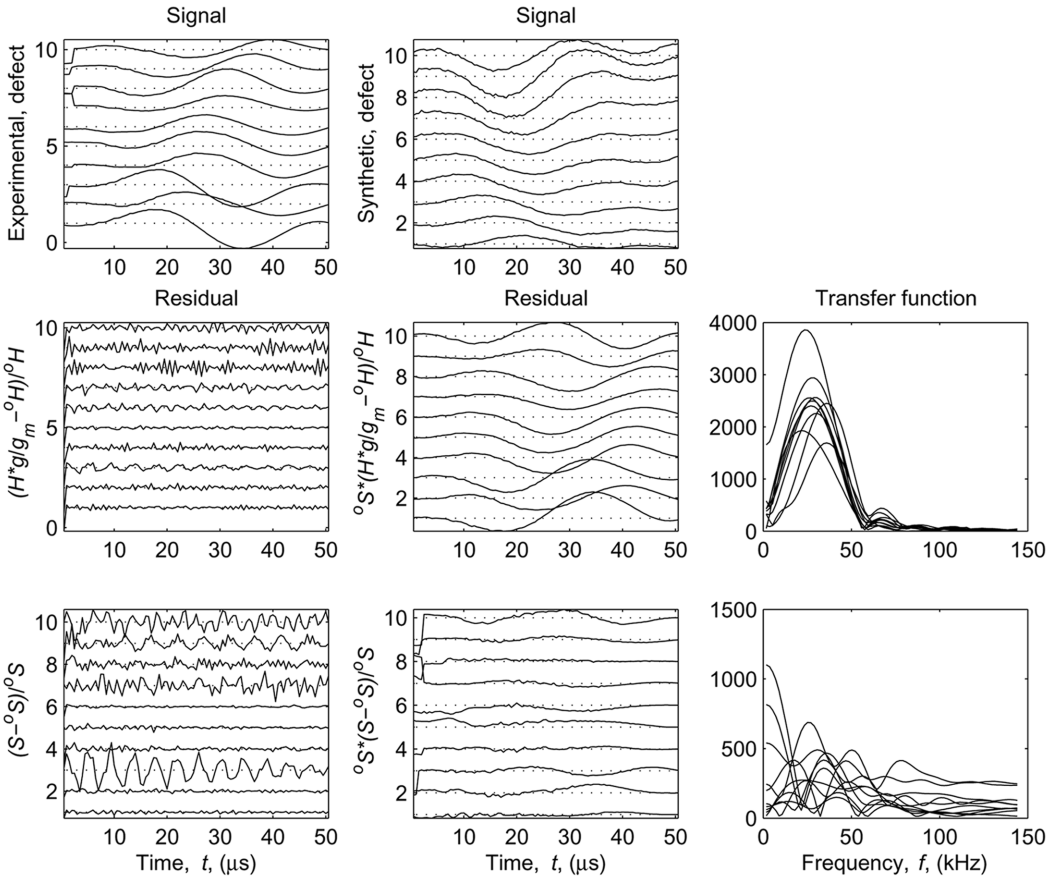

(a) Time window: 50 μs

Fig. 9 Variation of the fitness function for different parameters. The 1-10 numbering in the vertical axis represents the impact point label. The amplitude is adimensional

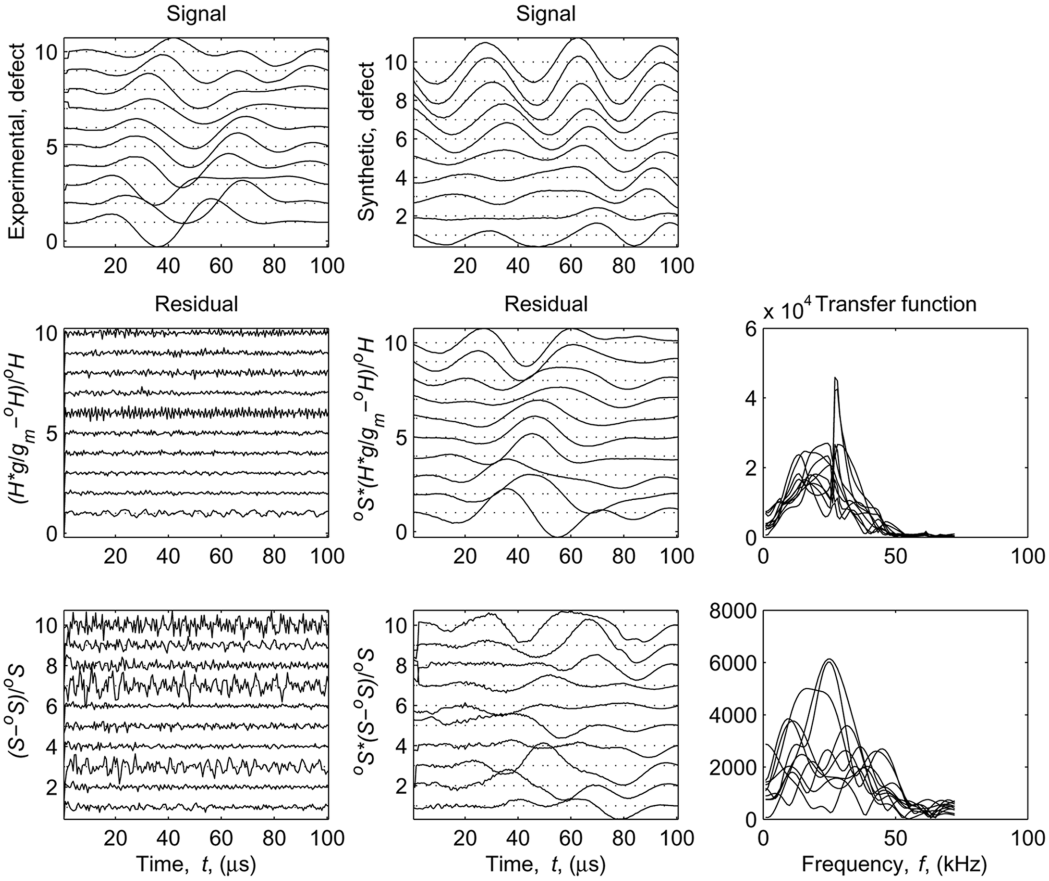

(b) Time window: 100 μs

Fig. 9 Continued

outlyers). Moreover, 0 – 100 μs allows sufficient time for the effect of the defect to be present in the signals, but not too much time to allow for numerical and noise-based deviations. The variation of the fitness function with the position of the defects is shown in Fig. 10. The position of the real defect, which is marked at coordinates (6,6), and the minimum value (white) of the cost functional should correlate.

The superaboundant calibrated signal allows to generate a map of probability of the defect by means of the cost functional. Several local minima appear as shown in Fig. 10, and the absolute minimum can be improved to overcome the effect of unknown parameters, the reduced number of measurements and the noise. The abovementioned local minima can be sources of false positive results, and need improvement. In the next section, the user defined filter W is used to bring some improvement. However, there are other candidates to be improved, such as the boundary conditions of the model, which are probably not perfect, the use of lighter accelerometers to reduce the structure-sensor interaction, and refining the mechanical properties uncertainties.

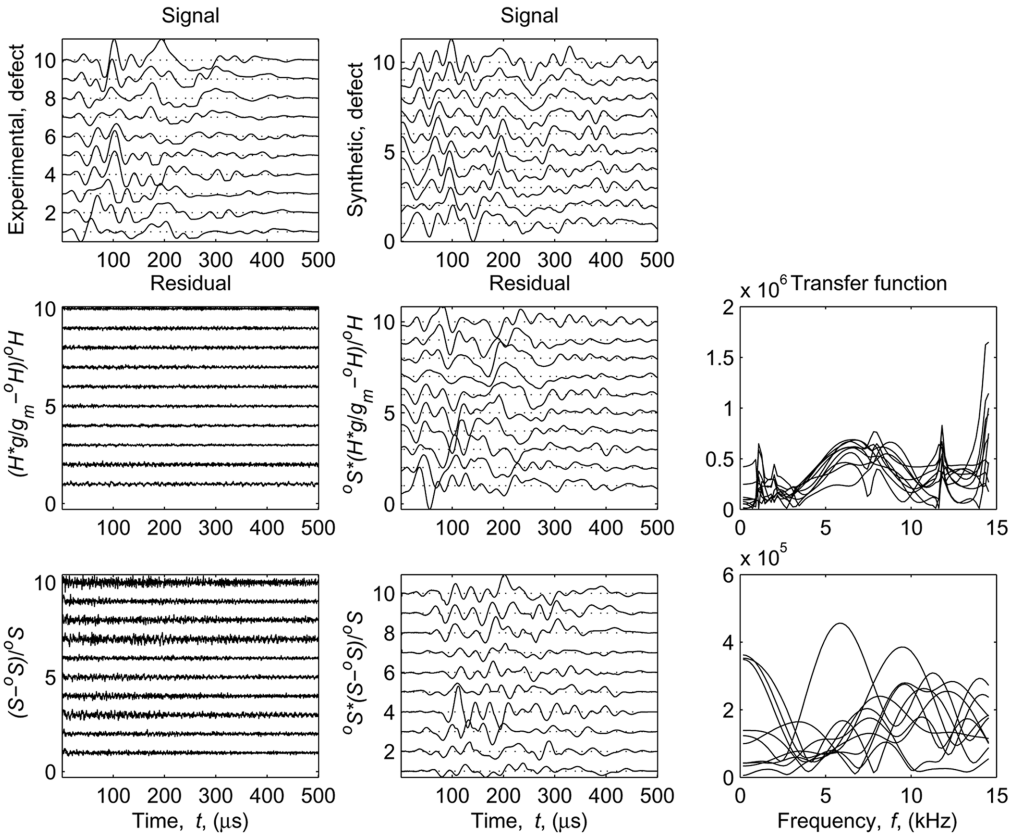

(c) Time window: 500 μs

Fig. 9 Continued

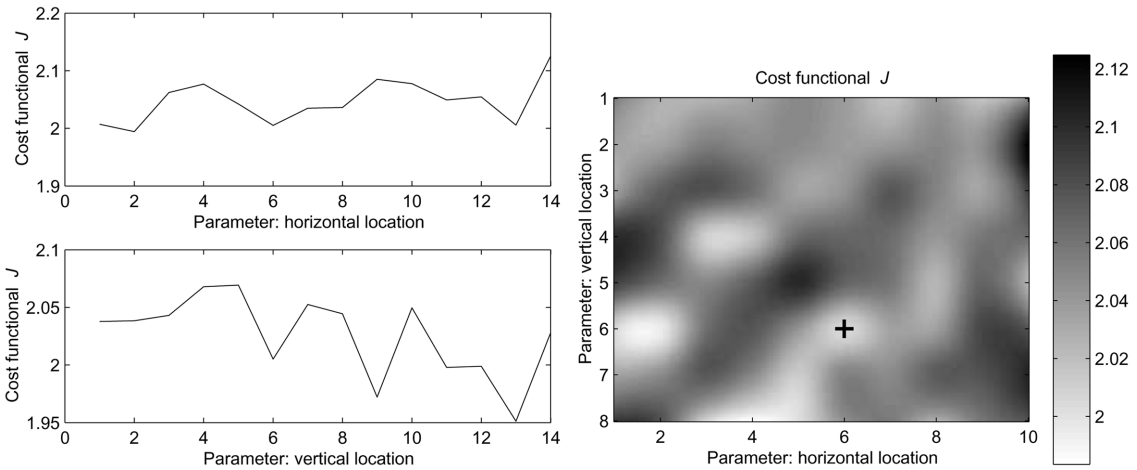

Fig. 10 Variation of the fitness function for two parameters: horizontal and vertical position of the defect, provided a fixed size of the defect at its true value (known size). Left: variation of one position parameter while the other one is fixed at the true value. Right: variation for both position parameters simultaneously

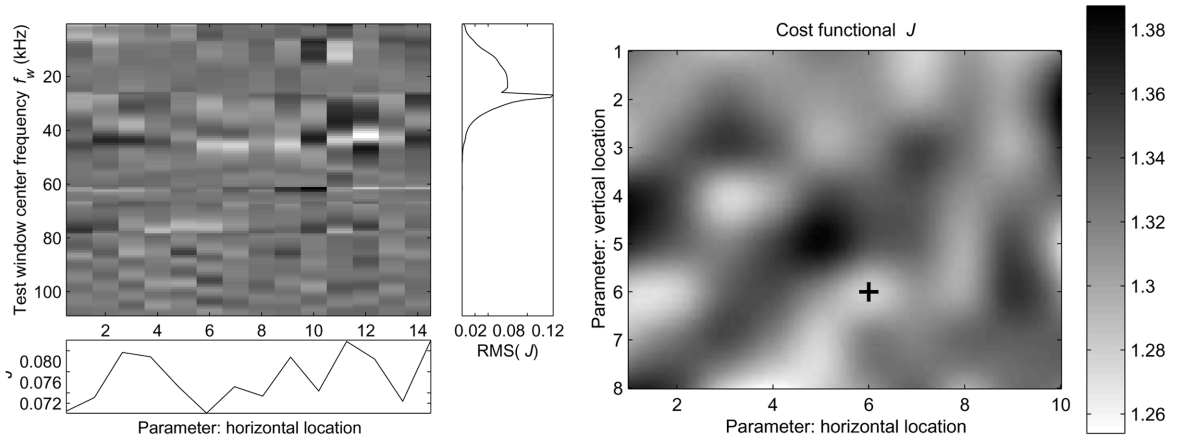

Fig. 11 Variation of the fitness function J. Left: variation of J with the horizontal position of the defect, and for a range of values of the center f_w of the frequency window and bandwidth of b = 0.91 kHz. Right: for two parameters, and cost functional defined with a $\cos^2$ window with central frequency f_w = 29.8 kHz chosen from the maximum of the previous $RMS(J)$

5.4 Evaluated frequency window

The cost functional can be defined with a weighting function along the frequency range that is integrated. Fig. 11 shows the dependency of the variation of the fitness with the horizontal parameter at a range of values for f_w. Two choices of frequency window have been made: (1) A Gaussian frequency window centered at a frequency f_w and with a bandwidth (variance) of $f_w/2$ and (2) A frequency window $W(f)$ defined using a central frequency f_w and a bandwidth b as,

$$W(f) = \begin{cases} 0 & 0 < f < f_w - b \\ \cos\left(\dfrac{f}{\pi \dfrac{f - f_w}{2b}}\right)^2 & f_w - b < f < f_w + b \\ 0 & f_w + b < f \end{cases} \tag{38}$$

The variation of the fitness function with the position of the defects is shown in Fig. 11 for the $\cos^2$ window. The use of a filter W allows to increase the contrast of the image from 2.12:2.00 = 6% to 1.38:1.26 = 10% as shown in Fig. 11.

6. Conclusions

A method for evaluation of defects using frequency domain information has been developed and tested experimentally. The key principles used can be summarized as follows.

1. The noise problem is dealt with by a strong regularization scheme such as the parametrization, besides not leaving aside any of the information gathered during the measurement.

2. A filtering window is applied to the residual to be minimized in order to reduce the components of information that may contain a higher signal to noise ratio.
3. A developed finite element code is used in this study as a convenient tool for solving the forward problem of modeling the wave propagation in the plate excited by impact loading.
4. A calibration in both amplitude and time domain, in addition of the presence of superabundant measurements allows to play with unknown parameters, such as the exact wavespeed (which usually carries some degree of variability), the actual impact applied force history, and the response of the accelerometer. The experimental results show that the search algorithm is robust against these uncertainties and uctuations.
5. A synthetic array of actuators is used to generate the excitation. The excitation array allows to add one more dimension to the set of measurement data, and hence enriching it. This array is synthesized by repeating one by one a virtually identical excitation at a set of different locations with a specifically built impactor device, instead of building and triggering the complete set of actuators at the same experiment.

The performance of the developed method for an experimental test on a clamped steel plate is not fully satisfactory as several local minima in the cost functional may lead to a wrong damage characterization. The origin of this lack of precision in the output is thought to be related to a mismatch between experimental and synthesized signal by FEM. However, the inverse problem is capable to reconstruct the defect location despite the divergence. There may be several reasons for the mismatch in signals: a partial clamping in the experimental specimen, an interaction between the accelerometer weight and the specimen, and a mismatch between accelerometer response frequency and vibration spectrum excited by the impact event.

To answer this, we have proposed several methods to overcome the difficulty of identification from defective measurements, only one measuring accelerometer and few impact events, in addition to the uncertainty in the exact value of the material properties and the predominance of noise. However, more advanced studies should be carried out for individual damage cases. In addition, the sensitivity of the range of frequencies excited by the impactor increases the need for further developing the algorithms for better experimental efficiency.

Acknowledgements

This work was supported by the Fulbright Foundation and the Ministerio de Educación Cultura y Deporte for the postdoctoral fellowship FU2002-0442.

References

Au, F.T.K., Cheng, Y.S., Tham, L.G. and Bai, Z.Z. (2003), "Structural damage detection based on a micro-genetic algorithm using incomplete and noisy modal test data", *J. Sound Vib.*, **259**(5), 1081-1094.

Bathe, K.J. (1996), *The Finite Element Procedures in Engineering Analysis*, Prentice Hall, Englewood Cliffs, NJ.

Bernal, D. (2002), "Load vectors for damage localization", *J. Eng. Mech.*, **128**(1), 7-14.

Boström, A., Johansson, G. and Olsson, P. (2001), "On the derivation of a hierarchy of dynamic equations for a homogeneous, isotropic, elastic plate", *Int. J. Solids Struct.*, **38**, 2487-2501.

Chou, J.-H. and Ghaboussi, J. (2001), "Genetic algorithms in structural damage detection", *Comput. Strut.*, **79**, 1335-1353.

Christides, S. and Barr, A.D.S. (1984), "One-dimensional theory of cracked bernulli-euler beams", *Int. J. Mech. Sci.*, **26**, 639-648.
Dennis, J.E. Jr. and Schnabel, Robert B. (1983, 1996), *Numerical Methods for Unconstrained Optimization and Nonlinear Equations*. SIAM, Philadelphia.
Eriksson, A.S., Boström, A. and Datta, S.K. (1995), "Ultrasonic wave propagation through a cracked solid", *Wave Motion*, **22**, 297-310.
Friswell, M.I. and Penny, J.E.T. (1997), Is damage localization using vibrational measurement practical? *In Proc. Int. Workshop on Structural Damage Assessment using Advanced Signal Processing Procedures*, pp.351-362, June/July.
Friswell, M.I., Pennyb, J.E.T. and Garvey, S.D. (1998), "A combined genetic and eigensensitivity algorithm for the location of damage in structures", *Comput. Struct.*, **69**, 547-556.
Gudmudson, P. (1982), "The dynamic behaviors of slender structures with cross section cracks", *J. Mech. Phys. Solids*, **31**(4), 329-345.
Kawchuk, G.N. and Elliott, P.D. (1998), "Validation of displacement measurements obtained from ultrasonic images during indentation testing", *Ultrasound Med. Biol.*, **24**(1), 105-111.
Kim, B.H., Joo, H.J. and Park, T.H. (2006), "Nondestructive damage evaluation of a curved thin beam", *Struct. Eng. Mech.*, **24**(6), 665-682.
Kimoto, K. and Hirose, S. (2000), A numerical modelling of contact sh-wave transducers. In D.O. Thompson and D.E. Chimenti, editors, *Review of Progress in Quantitative Nondestructive Evaluation, Vol. 20*.
Krawczuk, M. (2002), "Application of spectral beam finite element with a crack and iterative search technique for damage detection", *Finite Elem. Anal. Des.*, **38**, 537-548.
Lee, S.Y. and Wooh, S.C. (2005), "Waveform-based identification of structural damage using the combined fem and microgenetic algorithms", *J. Struct. Eng.,* ASCE, **131**(9), 1464-1472.
Li, Y.Y., Cheng, L., Yam, L.H. and Wong, W.O. (2002), "Identification of damage locations for plate-like structures using damage sensitive indices: Strain modal approach", *Comput. Struct.*, **80**, 1881-1894.
Liu, P.L. and Chen, C.C. (1996), "Parametric identification of truss structures by using transient response", *J. Sound Vib.*, **191**(2), 273-287.
Maeck, Johan, Peeters, Bart and Roeck, Guido De (2001), "Damage identification on the Z24 bridge using vibation monitoring", *Smart Mater. Struct.*, **10**, 512-517.
Mares, C. and Surace, C. (1996), "An application of genetic algorithms to identify damage in elastic structures", *J. Sound Vib.*, **195**, 195-215.
Marty, P.N., Lowe, M.J.S. and Cawley, P. (2000), Finite element predictions of guided ultrasonic wave fields generated by piezoelectric transducers. In D.O. Thompson and D.E. Chimenti, editors, *Review of Progress in Quantitative Nondestructive Evaluation, Vol. 20*.
Miller, Ronnie K. (1986), *Nondestructive Testing Handbook*, Vol.5. American Society for Nondestructive Testing, 5 edition.
Rus, G., Wooh, S.C. and Gallego, R. (2004), "Analysis and design of wedge transducers using the boundary element method", *J. Acoustic Soc. Am.*, **115**, 2919-2927.
Rus, G., Lee, S.Y., Chang, S.Y. and Wooh, S.C. (2006), "Optimized damage detection of steel plates from noisy impact test", *Int. J. Numer. Meth. Eng.*, **68**, 707-727.
Schmerr, L.W. (1998), *Fundamentals of Ultrasonic Nondestructive Evaluation — A Modeling Approach*. Plenum Press, New York.
Suh, M.W., Shim, M.B. and Kim, M.Y. (2000), "Crack identification using hybrid neuro-genetic technique", *J. Sound Vib.*, **238**(4), 617-635.
Ren, Guido Wei-Xin abd Roeck, De (2002), "Structural damage identification using modal data. I: Simulation verification", *J. Struct. Eng.*, **128**(1), 87-95.
Wendel, R. and Dual, J. (1997), "Application of neural networks to quantitative nondestructive evaluation", *NDT & E Int.*, **30**(5), 325.
Wooh, S.-C., Clay, A. and Wei, C. (1997), Ultrasonic phased array transducers for nondestructive evaluation of steel structures. In Society of Experimental Mechanics, editor, *SEM Spring Conference, Bellevue, WA, Society for Experimental Mechanics, June 2Ü4*, pp.1-2.
Wooh, S.C. and Daniel, I.M. (1994), "Three dimensional ultrasonic imaging of defects and damage in composite

materials", *Mater. Eval.*, 1199-1206.
Wooh, S.C. and Zhou, Q. (2001), "Behavior of laser-induced ultrasonic waves radiated from a wet surface, Part I. Theory", *J. Appl. Phys.*, **89**(6), 3469-3477.
Xiang, Jiawei, He, Zhengjia, He, Yumin and Chen, Xuefeng (2007), "Static and vibration analysis of thin plates by using finite element method of b-spline wavelet on the interval", *Struct. Eng. Mech.*, **25**(5), 613-629.
Zhao, J., Gaydecki, P.A. and Burdekin, F.M. (1995), "A numerical model of ultrasonic scattering by a defect in an immersion test", *Ultrasonics*, **33**(4), 271-276.

Appendix

In the following, the proof of equivalence between time and frequency domain definitions of the cost functional J is made. Moreover, this proof provides a consistent definition of J in which two signals $f(t)$ and $g(t)(t = 0 - T)$ are compared. The functional is weighted by a generic function

$$\begin{aligned}
2TJ &= \int_0^T [w(t) * (f(t) - g(t))]^2 dt \\
&= \int_0^T \left(\sum_{j=-\infty}^{+\infty} W_j (F_j - G_j) e^{\frac{2\pi ijt}{T}} \right)^2 dt \\
&= \int_0^T \left(\sum_{j=-\infty}^{+\infty} \sum_{k=-\infty}^{+\infty} W_j (F_j - G_j) W_k (F_k - G_k) e^{\frac{2\pi i(j+k)t}{T}} \right) dt \\
&= \sum_{j=-\infty}^{+\infty} \sum_{k=-\infty}^{+\infty} W_j (F_j - G_j) W_k (F_k - G_k) \cdot \begin{Bmatrix} 1 & j+k=0 \\ 0 & j+k \neq 0 \end{Bmatrix} \\
&= \sum_{j=-\infty}^{+\infty} W_j (F_j - G_j) W_{-j} (F_{-j} - G_{-j}) \\
&= \sum_{j=-\infty}^{+\infty} W_j (F_j - G_j) \overline{W}_j (\overline{F}_j - \overline{G}_j) = \sum_{j=-\infty}^{+\infty} |W_j|^2 |(F_j - G_j)|^2 = 2TJ
\end{aligned} \tag{39}$$

where,

$$\overline{F}_j = \int_0^1 \overline{f}(t) e^{\frac{\overline{2\pi ijt}}{T}} dt = \int_0^1 f(t) e^{\frac{-2\pi ijt}{T}} dt = F_{-j} \tag{40}$$

For the discrete case we have a different procedure with the same conclusion

$$\begin{aligned}
2TJ &= \frac{T}{N} \sum_{i=1}^{N} [w(t_i) * (f(t_i) - g(t_i))]^2 \\
&= \frac{T}{N^3} \sum_{i=1}^{N} \left(\sum_{j=1}^{N} W(\omega_j)(F(\omega_j) - G(\omega_j)) e^{\frac{2\pi i(j-1)(i-1)}{N}} \right)^2 \\
&= \frac{T}{N^3} \sum_{i=1}^{N} \left(\sum_{j=1}^{N} \sum_{k=1}^{N} W(\omega_j)(F(\omega_j) - G(\omega_j)) W(\omega_k)(F(\omega_k) - G(\omega_k)) e^{\frac{2\pi i(j+k-2)(i-1)}{N}} \right) \\
&= \frac{T}{N^2} \sum_{j=1}^{N} W(\omega_j)(F(\omega_j) - G(\omega_j)) \overline{W}(\omega_j)(\overline{F}(\omega_j) - \overline{G}(\omega_j)) \\
&= \frac{T}{N^2} \sum_{j=1}^{N} |W(\omega_j)|^2 |F(\omega_j) - G(\omega_j)|^2 = 2TJ
\end{aligned} \tag{41}$$

where

$$\sum_{i=1}^{N} e^{\frac{2\pi i(j+k-2)(i-1)}{N}} = \begin{cases} N \Leftrightarrow j+k = 2+\alpha N \\ 0 \Leftrightarrow j+k \neq 2+\alpha N \end{cases} \tag{42}$$

The extension to the case of a synthetic array of impactors m or receivers n which can be weigthed by v_{mn}, and applied to the previously defined residual **R** yields

$$\begin{aligned} J &= \frac{1}{2T}\sum_{m,n} v_{mn}^2 J_{mn} \\ &= \frac{1}{2N}\sum_{m,n} \int_0^T [w(t) * v_{mn}(\tilde{h}_{mn}^{(IR)}(t) - h_{mn}^{(IR)}(t))]^2 dt \\ &= \frac{1}{2N^2}\sum_{m,n,j} |v_{mn} W(\omega_j)|^2 \left|\tilde{H}_{mn}^{(IR)}(\omega_j) - H_{mn}^{(IR)}(\omega_j)\right|^2 \end{aligned} \tag{43}$$